CFSRC COLLOQUIUM

Proceedings of the Cold-Formed Steel Research Consortium Colloquium
20-22 October 2020 (cfsrc.org)

Local-distortional interaction in cold-formed steel lipped channel beams under uniform bending: Experimental investigation

Man-Tai Chen[1], Ben Young[2], André Dias Martins[3], Dinar Camotim[4], Pedro Borges Dinis[5]

Abstract

This paper describes a test campaign concerning the behavior and strength of cold-formed steel (CFS) lipped channel (LC) beams experiencing local-distortional (L-D) interaction made of G450-G500 high-strength steel grades. This investigation involves the performance of 20 tests on simply supported beams arranged in a "back-to-back" configuration, subjected to four-point major-axis bending and laterally restrained at the loading points. All tested specimens failed in the expected L-D interactive modes and exhibited critical distortional-to-local buckling moment ratios ranging between 1.09 and 1.46 (i.e., prone to "true L-D interaction"). The experiment results obtained and reported consist of beam (i) moment-displacement equilibrium paths, (ii) photos evidencing the evolution of the beam deformed configurations along those equilibrium paths (including the failure modes) and (iii) failure moments – it is found that these results are in good agreement with recently performed numerical simulations. Finally, the experimental failure moments obtained are compared with their estimates provided by the (i) currently codified Direct Strength Method (DSM) strength curves associated with local and distortional failures, and (ii) other available DSM-based design approaches developed to handle L-D interactive failures. This comparison provides solid evidence that the CFS specifications must include a DSM-based design approach able to handle beam L-D interactive failures – the current local and distortional design curves clearly overestimate all the experimental failure moments.

1. Introduction

The technological advances in the metal alloy production led to the development of high-strength steels, thus enabling the use of structural elements with thinner walls which, naturally, provide more economic design solutions (due to the higher strength-to-weight ratios). These advances make it now feasible to use cold-formed steel (CFS) structural systems formed by members with extremely thin walls and, therefore, intrinsically more susceptible to several instability phenomena, namely local (L), distortional (D) and global (G) buckling, or also any coupling phenomenon involving them [1] (*e.g.*, L-D interaction).

The research activity on the influence of L-D interaction on the behavior and strength of CFS members involved almost solely columns – indeed, the number of studies devoted to this coupling phenomenon in CFS beams is fairly scarce. Next, the currently available publications are briefly reviewed and discussed – for organizational purposes, numerical and experimental investigations are addressed separately.

Silvestre *et al*. [2] reported an ABAQUS shell finite element (SFE) study on simply supported CFS LC beams uniformly bent about the major-axis, which involved 90 beams critical local-to-distortional buckling moment ratios (M_{crL}/M_{crD}) ranging between 0.85 and 1.20. It was concluded that, in general, the current Direct Strength Method (DSM) local and distortional design curves yield unsafe failure moment predictions. A bit later, Dinis & Camotim [3] also reported another ABAQUS SFE investigation, now concerning the elastic and elastic-plastic post-buckling behavior of simply supported CFS LC beams under uniform bending and such that $M_{crD}/M_{crL} \cong 1.0$ – two mechanically distinct beam types were considered, differing in the wall triggering local instability: either (i) the compressed flange or (ii) the web. It was shown that their post-buckling behaviors are qualitative and quantitatively distinct, with the latter beams exhibiting a fair amount of elastic-plastic strength reserve (i.e., a post-buckling behavior that strongly resembles, qualitatively, that of columns affected by L-D interaction). Much more recently, Anbarasu [4] reported another ABAQUS SFE investigation on simply supported CFS LC beams uniformly

[1] Assistant Professor, State Key Laboratory of Ocean Engineering, Department of Civil Engineering, Shanghai Jiao Tong University, mantai.chen@sjtu.edu.cn
[2] Full Professor, Department of Civil and Environmental Engineering, The Hong Kong Polytechnic University, ben.young@polyu.edu.hk
[3] Postdoctoral Researcher, CERIS, DECivil, Instituto Superior Técnico, Universidade de Lisboa, andrerdmartins@tecnico.ulisboa.pt
[4] Full Professor, CERIS, DECivil, Instituto Superior Técnico, Universidade de Lisboa, dcamotim@civil.ist.utl.pt
[5] Assistant Professor, CERIS, DECivil, Instituto Superior Técnico, Universidade de Lisboa, dinis@civil.ist.utl.pt

bent about the major-axis, but quite similar to the previous ones [2,3]. All beams analyzed evidenced L-D interaction and the author confirmed that the current DSM local and distortional DSM design curves [5] overestimate their failure moments, which led him to propose a new DSM-based strength curve to handle that L-D interactive failures – however, this design curve provides overly conservative and highly scattered failure moment estimates. On the other hand, Haidarali & Nethercot [6] developed two ABAQUS SFE models to analyze the complex behavior stemming from coupling phenomena (L-D interaction in particular) in CFS zed-section beams – the "4 point-bending" (loads applied at *L*/3 from the supports) experimental results reported earlier by Yu & Schafer [7,8] were used to calibrate the numerical models, one termed "complete" and the other "simplified". The latter model was subsequently employed to investigate the post-buckling behavior of zed-beams subjected to "4 point-bending", with the purpose of assessing the influence of the flange-to-lip width ratio and lip inclination/orientation [9]. It was shown that the former may alter significantly the beam post-buckling behavior and strength, and also influences the "transition" between local, combined local-distortional and distortional buckling. Haidarali & Nethercot [10] then extended the previous investigation in order to assess how the size and location of compressed flange intermediate "rounded stiffeners" influence the beam structural response. About two decades ago, Schafer [11] had already reported numerical evidence of L-D interaction in some of the 60 simply supported zed-beams under major-axis bending analyzed (although L-D interaction was outside the focus of the work). Much more recently, Martins *et al*. [12] reported an ABAQUS SFE investigation on CFS simply supported uniformly bent beams with three cross-section shapes (lipped channels, zed-sections and hat-sections) and two end support conditions. This parametric study involved 43 geometries per cross-section shape and 11 yield stress values, thus ensuring different M_{crD}/M_{crL} ratios and slenderness values, which makes it possible to capture/analyze three remarkably distinct L-D interaction types: "true L-D interaction" and "secondary local or distortional bifurcation L-D interaction". Design considerations were also reported, (i) confirming once more the inadequacy of the current DSM local and distortional design curves in predicting the failure moments[6], and (ii) proposing preliminary DSM-based design curves to capture the strength erosion due to the coupling phenomenon under consideration. Finally, Martins *et al*. [14] have very recently reported an in-depth investigation, based on Generalized Beam Theory (GBT) geometrically non-linear analyses, aimed at assessing the mechanics underlying the behavior of simply supported LC beams under uniform major-axis bending undergoing "true" and "secondary local or distortional-bifurcation" L-D interaction.

Concerning experimental investigations on L-D interaction, Bernard *et al*. conducted in the 90's, at the University of Sydney, tests on simply supported trapezoidal steel decks subjected to uniform minor-axis bending and exhibiting compressed flanges with "v" [15] (18 beams) or "flat-hat" [16] (9 beams) intermediate stiffeners. Since the cross-section and stiffener dimensions were "*selected to exhibit a variety of buckling modes, ranging from local and distortional*", several specimens tested (14 out of 27) showed clear evidence of L-D interaction. Much later, Wang & Zhang [17] reported a mostly experimental study on CFS C-section beams with several lip configurations (upright, inclined and return), comprising 12 specimens under uniform ("4-point") bending and 12 specimens under non-uniform ("3-point") bending. Several failure mode natures were observed, namely local, distortional and L-D interactive failures – 13 of the 24 specimens collapsed in L-D interactive modes. These authors confirmed the detrimental effects stemming from this coupling phenomenon: "*the interaction between local and distortional buckling may result in a detrimental effect on the bending strength of specimens*". Five years later, Wang & Young [18] also performed an experimental (and numerical) investigation on CFS beams bent about the major-axis under "4-point" and "3-point" bending and exhibiting three cross-sections – the 2 web-stiffened lipped channel specimens failed into L-D modes. It is also worth noting early work by Douty [19] and Serrete & Peköz [20] on simply supported standing seam roof panels with several configurations – the experimental results (tests carried out at the University of Cornell), showed evidence of L-D interaction and prompted the authors to propose design rules accounting for this coupling phenomenon. Finally, Ye *et al*. [21] conducted very recently, at the University of Sheffield, a "4-point" bending experimental investigation on CFS simply supported LC beams susceptible to L-D interaction – 6 "back-to-back" tests involving 3 distinct LC cross-sections were performed. The authors compared the failure moments obtained with their estimates provided by the current European, North American and other available (not codified) DSM-based design rules. They concluded that the predictions of the first two design rules are in good agreement with the experimental failure moments, which are underestimated by the DSM-based NLD and NDL design approaches – these quite surprising findings (note that the DSM-based design approaches were developed with the specific purpose of handling L-D interaction) will be discussed in Section 4.

This paper presents a carefully planned and executed experimental test campaign stemming from the collaboration between researchers from The University of Hong Kong, The Hong Kong Polytechnic University and the University of Lisbon. It is aimed at investigating the behavior and ultimate strength of CFS simply supported LC beams undergoing L-D

[6] At this stage, it is worth noting that Martins *et al*. [13] recently showed that the current DSM beam distortional design curve may lead to large failure moment overestimations in the moderate and high slenderness ranges – to improve this situation, these authors developed, validated and proposed a novel DSM-based strength curve against CFS beam distortional failures.

interaction. 40 LC specimens, made of zinc-coated G450 and G500 high-strength steel sheets, were employed to perform 20 "4-point" bending tests, ("back-to-back" configurations with lateral restraints at the loading points). The beam geometries were carefully selected to enable testing beams susceptible to "true L-D interaction". Tensile coupon tests were carried out to determine the specimen material properties and the initial geometrical imperfections were measured prior to testing. The results obtained and reported consist of beam (i) moment-displacement equilibrium paths, (ii) photos showing beam deformed configurations along those paths (including the failure modes) and (iii) failure moments. Finally, the experimental failure moments obtained are compared with their estimates yielded by several Direct Strength Method (DSM) [22-24] design curves: (i) the codified local and distortional ones and (ii) other available (not codified) curves developed for L-D interactive failures.

2. Beam Geometry Selection

The first step of an experimental investigation on LC beams affected by L-D interaction consists of carefully selecting/determining geometries (cross-section dimensions and span lengths) prone to this coupling phenomenon. Since the number of available results (namely failure moments) concerning the behavior and strength of beams collapsing in L-D interactive modes is rather scarce, it was decided to carry out an experimental investigation involving only LC beams undergoing "true L-D interaction", *i.e.*, with very close distortional (M_{crD}) and local (M_{crL}) critical buckling moments, *i.e.*, $R_{DL}=M_{crD}/M_{crL}\cong 1.0$. As discussed in Section 3.3, the fact that the beams are laterally restrained at the loading points prevents the occurrence of a "triple interaction" involving also (global) lateral-torsional buckling. In order to reach the sought beam specimen geometries, the selection procedure had to satisfy the following requirements/conditions:

(i) Specimen span lengths between 1000 and 2600mm (testing machine limitation).

(ii) Specimens without small lip widths (manufacturing limitation).

(iii) Thickness values and steel grades of t=1.0mm (G550), t=1.2mm (G500) or t=1.5mm (G450).

(iv) Failure loads (P_{Exp}) not exceeding 900kN (load actuator capacity) – although these beams may exhibit a significant post-critical strength (see, *e.g.*, [12]), the specimen failure moments are always well below the actuator capacity – the maximum critical buckling load is about 21.6kN, as discussed next.

(v) Preclude shear buckling in the vulnerable spans, *i.e.*, the web regions comprised between the end supports and the points of load application.

(vi) Preclude web-crippling failure due to stress concentrations in both the (vi_1) bottom flange and web regions, near the supports (EOF), and (vi_2) top flange and web regions, under the applied loads (IOF).

It should be mentioned that the requirements described in items (v) and (vi) were met by satisfying the design rules prescribed by EC3-1-5 [25] and EC3-1-3 [26], respectively. Due to the rather complex structural arrangement required to perform the 4-point bending tests, the beam selection procedure was carried out by means of a "trial-and-error" approach involving ABAQUS [27] shell finite element analyses that account for the actual test set-up. The models employed neglect the lipped channel rounded corners, for the sake of simplicity, and adopt commonly used Young's modulus and Poisson's ratio values, namely E=210GPa and ν=0.30. Their main characteristics are the following:

(i) Discretization. The lipped channel beam mid-surface is discretized into fine meshes of S4 (ABAQUS nomenclature) shell finite elements, *i.e.*, a 4-node isoparametric shell element with shear stiffness obtained by a full integration rule. Due to the symmetry conditions, only one beam is modeled.

(ii) Material Model. Linear elastic.

(iii) Loading. Two vertical concentrated forces are applied in the intersection of the horizontal plane (X0Z) containing the top/compressed flange and a vertical line (along Y) passing through the lipped channel shear center, at a distance L/4 from the end supports (see Fig. 1(a)).

(iv) Boundary Conditions. The beam end support conditions are simply supported, *i.e.*, the transverse displacements (along X and Y – see Fig. 1(a)) of all end cross-section nodes are prevented, as well as the rotations along Z (twisting).

(v) Constraints. Since transfer plates were installed at the loading points (as discussed in Section 3.3), a coupling constraint was used to associate the values of all d.o.f.s corresponding to nodes in the transfer plate regions (see Fig. 1(a)) to the respective (reference) loading point nodes.

(vi) Stiffening plates. In order to prevent web-crippling and shear buckling, 10mm thick and 90mm wide steel stiffening plates were employed in the web region at the loading point locations (see Fig. 1(a)).

Table 1 shows the output of this selection procedure, satisfying items (i)-(vi) described above – it provides the obtained (i) cross-section mid-line dimensions (b_w, b_f, b_l – web, flange, lip widths), thickness (t) and span length (L), (ii) critical local (M_{crL}) and distortional (M_{crD}) buckling moments, (iii) critical distortional half-wave number (given inside brackets in the M_{crD} column), (iv) R_{DL} values and (v) local (λ_L) and distortional slenderness (λ_D) values. A total of 18 distinct geometries were selected, exhibiting R_{DL} values comprised between 1.04 and 1.36. With three exceptions, all the specimens selected have nominal wall thickness t=1.5mm (G450) – the exceptions are the specimens labelled LC10, LC17 and LC18, which have t=1.2mm (G500). Moreover, all specimens exhibit one critical distortional half-wave and have local buckling triggered by the top/compressed

Table 1: Selected LC beam specimen geometries (mid-line dimensions), critical local and distortional buckling moments (as well as their ratios), and local and distortional slenderness

Specimen	b_w (mm)	b_f (mm)	b_l (mm)	t (mm)	L (mm)	M_{crL}(kNcm)	M_{crD} (kNcm)	R_{DL}	λ_L	λ_D
LC1	130	120	12	1.5	1800	439	568(1)	1.29	1.89	1.66
LC2	130	120	12	1.5	2200	435	507(1)	1.17	1.90	1.76
LC3	150	130	12	1.5	2200	467	574(1)	1.23	2.05	1.85
LC4	150	130	12	1.5	2600	464	515(1)	1.11	2.06	1.96
LC5	130	120	12	1.5	2600	433	473(1)	1.09	1.90	1.82
LC6	170	130	12	1.5	2600	536	598(1)	1.12	2.06	1.95
LC7	170	110	12	1.5	2600	656	683(1)	1.04	1.75	1.72
LC8	190	130	12	1.5	2600	611	690(1)	1.13	2.06	1.94
LC9	190	130	12	1.5	2200	619	802(1)	1.30	2.05	1.80
LC10	170	100	12	1.2	2600	380	462(1)	1.22	2.04	1.85
LC11	210	150	12	1.5	2600	585	743(1)	1.27	2.36	2.10
LC12	210	130	12	1.5	2600	686	791(1)	1.15	2.07	1.93
LC13	230	160	12	1.5	2600	609	828(1)	1.36	2.51	2.15
LC14	230	140	12	1.5	2600	699	883(1)	1.26	2.22	1.98
LC15	230	120	12	1.5	2600	817	935(1)	1.14	1.95	1.82
LC16	130	110	12	1.5	2600	482	514(1)	1.07	1.74	1.69
LC17	130	110	12	1.2	2600	249	323(1)	1.30	2.23	1.96
LC18	130	100	12	1.2	2600	281	355(1)	1.26	2.02	1.80

flange. For illustrative purposes, Fig. 1(b) displays the beam "signature curve" (M_{cr} vs. L) concerning the cross-section LC1, while Fig. 1(c) shows critical local and distortional buckling modes of the L=1800mm beam, which exhibits a R_{DL} value close to 1.0. Since the transfer plates located at the loading points restrain their in-plane and out-of-plane rotations, the "signature curve" is qualitatively very similar to that exhibited by fixed-ended members (see Fig. 1(b)). Moreover, the critical buckling mode shapes displayed in Figs. 1(c_1)-(c_2) show that only the beam central region buckles (as intended).

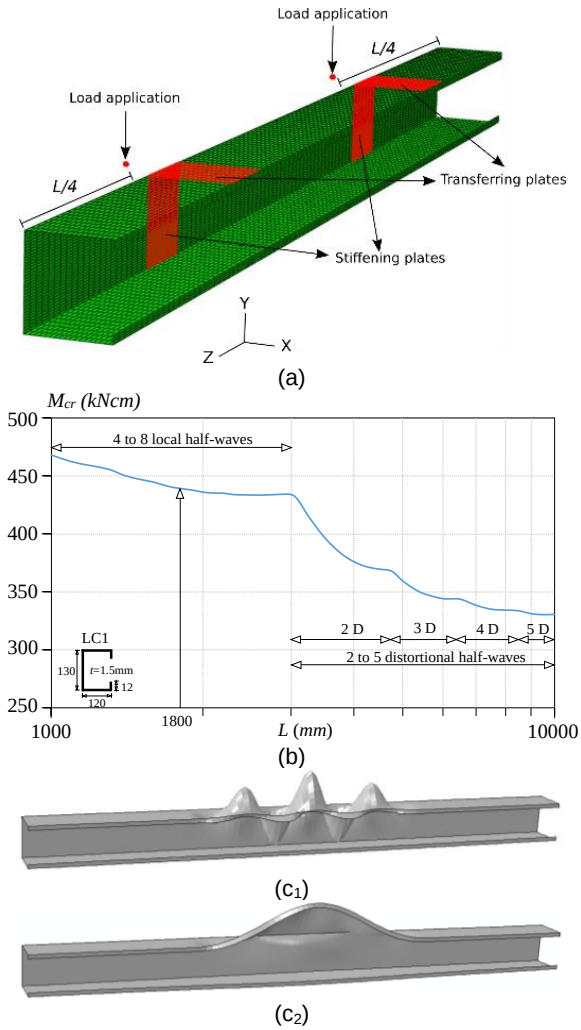

Figure 1: LC1 beam: (a) shell finite element model, (b) "signature curve" and (c) critical ($_1$) local and ($_2$) distortional buckling mode shapes (L=1800mm)

3. Experimental Investigation

3.1 Test specimens

A total of 40 CFS lipped channel beam specimens were tested under 4-point major-axis bending – two applied loads equally distant from the beam end supports, which means that the central span is under uniform bending moment. Moreover, in order to avoid load eccentricities, each test involves two identical "back-to-back" lipped channels, hereafter, termed lipped channels 'a' and 'b' – the loads are applied in the vertical plane containing the web mid-line of the "double lipped channel" cross-section, thus avoiding twisting (recall that, due to the single symmetry, the shear centre of an isolated lipped channel is located far away from its web mid-line). Therefore, a total of 20 beam tests were carried out.

The CFS test specimens were brake-pressed from high strength zinc-coated grades G450 and G500 structural steel sheets with nominal yield stresses of 450 and 500MPa, respectively. Note that these high-strength steel grades comply with the specifications of the Australian standard AS 1397-2011 [28]. The specimen nominal web widths (D) and flange widths (B) (see the definitions/nomenclature in Fig. 2(a))

ranged between 130 and 230mm, 100 and 160mm, respectively, and the lip widths (B_l) were equal to 13mm – recall that the nominal plate thickness (t) is either 1.2 or 1.5mm. The base metal thickness (t^*) was measured after removing the zinc coating by acid-etching – on each side of the section, the thickness of the zinc coating was 28.5μm for t=1.2mm and 27.5μm for t=1.5mm. The lipped channels were cut into different lengths of 1890mm, 2290mm and 2690mm, such that their planned (Section 2) full spans (L) equal 1800mm, 2200mm and 2600mm, respectively. Moreover, (i) the length of the beam central segment (L_m), located between the two loading points and under uniform bending, was taken as half of the full spans, while (ii) the two outer segments, vulnerable to shear buckling, have length L_s equal to a quarter of the full span and are located between the end supports and adjacent loading points. The measured cross-section dimensions (D, B, B_l, t, t^*, r_i – see Fig. 2(a)) and span lengths (L_m, L_s, L) of each specimen are given in Table 2 – note that, in order to assess the reliability of the test procedure, two groups of four specimens with similar dimensions were considered: LC8-(a+b+aR+bR) and LC14-(a+b+aR+bR). While specimens LC10-a, LC10-b, LC17-a, LC17-b, LC18-a, LC18-b, fabricated from one steel batch, have nominal plate thickness equal to 1.2mm (steel grade G500), the remaining 34 specimens, also fabricated from the same steel batch, have a higher nominal plate thickness (1.5mm – steel grade G450).

Table 2: Measured cross-section dimensions and span lengths of the 40 tested lipped channel beam specimens (dimensions in mm)

Specimen	D	B	B_l	t	t^*	r_i	δ_D	L_m	L_s	L
LC1-a	130.2	119.5	13.2	1.54	1.49	0.71	-1.3	900	450	1800
LC1-b	130.2	119.5	13.6	1.55	1.50	0.70	0.8	900	450	1800
LC2-a	130.1	119.9	13.3	1.56	1.50	0.70	1.3	1100	550	2200
LC2-b	130.6	119.1	13.9	1.55	1.50	0.70	1.8	1100	550	2200
LC3-a	150.7	129.4	13.3	1.55	1.49	0.71	1.5	1100	550	2200
LC3-b	150.3	129.4	13.5	1.56	1.50	0.69	0.8	1100	550	2200
LC4-a	150.6	129.0	14.0	1.54	1.49	0.71	2.3	1300	650	2600
LC4-b	150.6	129.2	13.9	1.55	1.50	0.70	2.4	1300	650	2600
LC5-a	130.7	119.6	13.6	1.54	1.49	0.71	2.4	1300	650	2600
LC5-b	130.4	119.4	13.6	1.54	1.49	0.71	2.0	1300	650	2600
LC6-a	170.5	129.1	13.8	1.55	1.49	0.71	1.9	1300	650	2600
LC6-b	170.7	129.0	13.6	1.53	1.48	0.72	2.3	1300	650	2600
LC7-a	170.7	109.2	13.8	1.55	1.49	0.71	1.4	1300	650	2600
LC7-b	170.5	109.3	13.6	1.54	1.49	0.71	1.8	1300	650	2600
LC8-a	189.9	129.8	13.8	1.54	1.49	0.71	1.8	1300	650	2600
LC8-b	190.0	129.7	13.7	1.54	1.49	0.71	2.0	1300	650	2600
LC8-aR	190.2	129.9	12.8	1.55	1.49	0.70	0.1	1300	650	2600
LC8-bR	190.3	129.5	13.2	1.55	1.49	0.71	0.8	1300	650	2600
LC9-a	190.3	129.2	13.7	1.56	1.50	0.70	0.5	1100	550	2200
LC9-b	190.2	129.4	13.3	1.55	1.49	0.70	0.5	1100	550	2200
LC10-a	170.0	101.1	13.1	1.24	1.19	0.76	0.3	1300	650	2600
LC10-b	170.5	101.3	12.9	1.24	1.18	0.76	0.5	1300	650	2600
LC11-a	207.5	150.1	13.7	1.52	1.47	0.73	-0.5	1300	650	2600
LC11-b	207.7	150.5	13.3	1.55	1.49	0.71	-0.8	1300	650	2600
LC12-a	210.7	129.7	13.7	1.55	1.50	0.70	1.6	1300	650	2600
LC12-b	210.4	129.8	13.4	1.54	1.49	0.71	1.4	1300	650	2600
LC13-a	230.5	159.9	13.4	1.53	1.47	0.72	1.8	1300	650	2600
LC13-b	230.8	159.3	13.5	1.54	1.48	0.71	1.3	1300	650	2600
LC14-a	230.5	139.8	13.4	1.52	1.47	0.73	1.3	1300	650	2600
LC14-b	230.5	139.6	13.2	1.55	1.49	0.71	1.3	1300	650	2600
LC14-aR	230.5	139.1	13.4	1.53	1.48	0.72	1.3	1300	650	2600
LC14-bR	230.4	139.1	13.3	1.55	1.49	0.71	1.0	1300	650	2600
LC15-a	230.8	119.4	13.5	1.55	1.49	0.70	1.3	1300	650	2600
LC15-b	230.4	119.6	13.4	1.55	1.49	0.71	1.0	1300	650	2600
LC16-a	130.4	109.7	13.3	1.54	1.48	0.71	1.9	1300	650	2600
LC16-b	130.4	109.6	13.3	1.54	1.48	0.71	1.9	1300	650	2600
LC17-a	130.9	111.1	12.9	1.24	1.18	0.76	0.8	1300	650	2600
LC17-b	130.1	111.0	13.1	1.25	1.20	0.75	0.3	1300	650	2600
LC18-a	129.3	100.9	13.5	1.25	1.20	0.75	-2.0	1300	650	2600
LC18-b	129.8	101.0	13.1	1.25	1.19	0.76	0.3	1300	650	2600

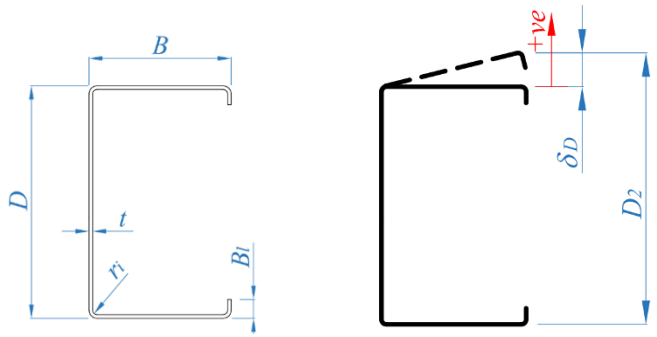

(a) (b)

Figure 2: Lipped channel cross-section (a) geometry and dimensions and (b) distortional initial geometrical imperfections at mid-span

3.2 Material properties

A series of tensile coupon tests were carried out to determine the material properties (Young's modulus, yield stress, ultimate tensile stress and ultimate strain) of the CFS lipped channel beam specimens. Since these specimens were fabricated from the same batch of steel, for cross-sections sharing the same nominal plate thickness and steel grade, two representative coupon specimens were extracted from the centre of the web (flat areas) in the longitudinal direction of specimens LC1-a and LC10-a. It is logical to expect the material properties obtained from specimens LC10-a and LC1-a to be similar to those exhibited by the other specimens with nominal plate thickness t=1.2mm and t=1.5mm, respectively.

The coupon dimensions considered are in accordance with the American standard ASTM-E8M [29] (tensile testing of metals), namely 12.5mm wide coupons of gauge length 50mm, and the coupon tests were carried out in a MTS displacement-controlled testing machine with friction grips. Before conducting these tests, an extensometer of 50mm gauge length was calibrated to measure the longitudinal strain of the coupon specimens. The measurements of the applied load and strains were recorded, by means of a data acquisition system, at regular intervals during the tests. In addition, the coupons were tested according to the recommendations of Huang & Young [30] for cold-formed carbon steel, *i.e.*, the loading procedure was paused for 100 seconds near the (i) 0.2% proof stress and (ii) ultimate tensile strength, to allow for the stress relaxation associated with plastic straining and to obtain the static stress-strain relationship. Table 3 shows the nominal and measured material properties obtained from the LC1-a and LC10-a specimen coupon tests, namely the values of Young's modulus (E), static 0.2% proof stress ($\sigma_{0.2}$), static tensile ultimate stress (σ_u) and elongation after fracture (ε_f).

Table 3: Nominal and measured material properties of the CFS lipped channel specimens LC1-a and LC10-a

Specimen	Nominal		Measured			
	t (mm)	$\sigma_{0.2}$ (MPa)	E (GPa)	$\sigma_{0.2}$ (MPa)	σ_u (MPa)	ε_f (MPa)
LC1-a	1.5	450	213.3	490.8	514.8	11.5
LC10-a	1.2	500	210.0	614.3	628.3	7.7

For illustrative purposes, Figs. 3(a)-(b) show the (test and static) stress-strain curves obtained from the coupon tests concerning specimens LC1-a and LC10-a, respectively – they exhibit "engineering" constitutive laws that are almost elastic perfectly-plastic (at least until up to $\varepsilon \cong 8\%$ and $\varepsilon \cong 6\%$, respectively – see Figs. 3(a)-(b)) and, naturally, also very similar to those obtained in another experimental investigation recently conducted by the authors on CFS columns affected by L-D interaction [31] (they were extracted from the same batch of steel).

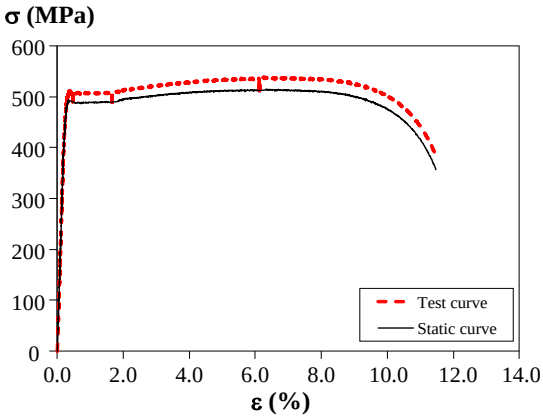

(a)

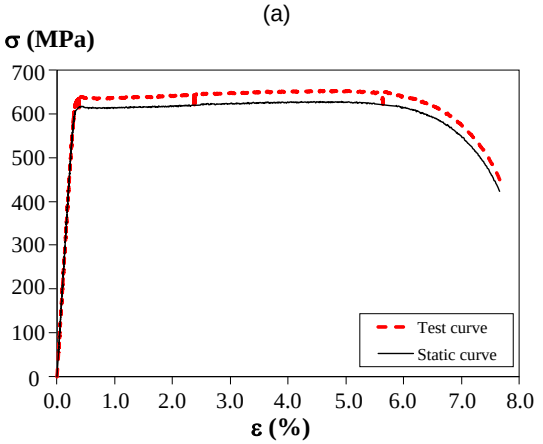

(b)

Figure 3: Tensile coupon tests: illustrative "engineering" stress-strain curves concerning specimens (a) LC1-a and (b) LC10-a

3.3 Test set-up and procedure

Four-point bending tests were conducted to investigate the behavior and ultimate strength of CFS lipped channel beam specimens under uniform major-axis moment acting on the central segment of length $L/2$. As mentioned previously, due to the cross-section single symmetry, each test involved two back-to-back "twin" lipped channel beams. Before conducting a test, holes with 8mm diameter were drilled on the lipped channel specimen flanges and web at four cross-section locations, namely those corresponding to the loading points and end support locations, in order to enable the installation of aluminum T-shaped blocks and stiffening plates. The two lipped channel

beams were then bolted to the T-shape aluminum blocks at the cross-section corresponding to the points of loading application and end supports. The beams were also stiffened at the above locations, by means of 90mm wide aluminum plates intended to prevent any possible web crippling and/or local bearing failure – note that, the twin lipped channel beams are mechanically independent, unlike in the tests reported in [21]. In addition, the T-shape aluminum blocks were bolted to the steel plates transferring the loads, in order to ensure uniformly distributed loads at both the loading points and end supports. Figs. 4(a)-(b) provide views of the aluminum T-shape block and stiffening plates at one beam end support.

Figs. 5(a)-(b) display a schematic representation and an overall view of the test rig and test set-up employed to perform the four-point bending tests. The beam end-cross sections are attached to rigid plates resting on cylindrical rollers, thus meaning that the beam is simply supported in the plane of loading (in-plane). The loading arrangement comprises an actuator that applies a vertical loading at the central region of a spreader beam, which then transfers it to the twin lipped channel beam, at cross-sections located $L/4$ from its end supports. The half-sphere allows only in-plane rotation and the cylindrical roller allows both in-plane rotation and translation. Figs. 5(a)-(b) make it possible to visualize the whole loading arrangement. Finally, it should be mentioned that the twin lipped channel beam is effectively laterally restrained at the two cross-sections located $L/4$ from its end supports.

(a)

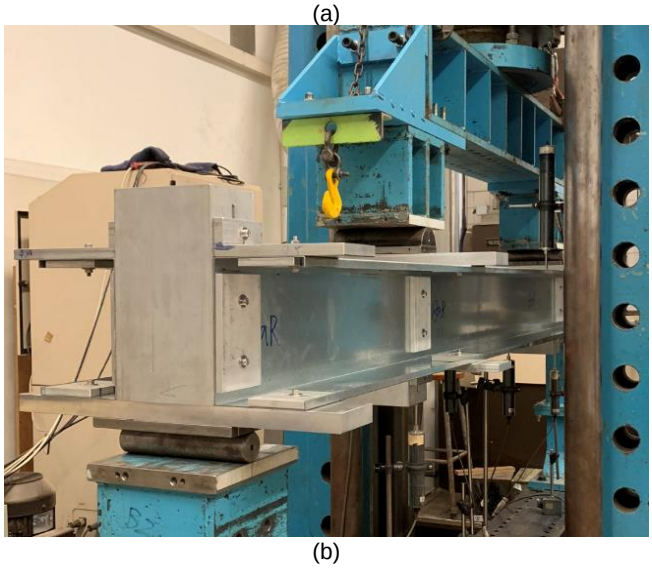

(b)

Figure 4: Installation of T-shape aluminum blocks and stiffening plates: (a)+(b) views of the installed T-shape aluminum block and stiffening plates

Figs. 5(a)-(b) also show the Linear Variable Displacement Transducer (LVDT) arrangement, consisting of six transducers (LVDT-1 to LVDT-6), four placed at the twin lipped channel specimen bottom flanges and two at its top flanges. The former are located (i) at each loading point (LVDT-1 and LVDT-2) and (ii) at the mid-span cross-section of each lipped channel beam (LVDT-3 and LVDT-4), 10mm away from the bottom flange-web corners. As for the latter (LVDT-5 and LVDT-6), they are located 15mm away from the top flange-lip corners. The vertical deflections measured by transducers LVDT-1 to LVDT-4 are used to obtain the bending curvature exhibited by each lipped channel specimen. On the other hand, the vertical deflections measured by transducers LVDT-3 to LVDT-6 make it possible to capture/determine the distortional deformations occurring at the twin lipped channel specimen mid-span cross-section (the one most likely to develop a plastic hinge associated with the collapse mechanism).

A displacement-controlled loading procedure was employed to drive the hydraulic actuator at a constant speed of 0.3mm/min for all beam tests. The use of displacement control made it possible to assess the beam geometrically non-linear behavior after the peak load/moment has been reached. The applied displacement was paused for 100 seconds at the ultimate load, in order to eliminate/reduce the strain-rate dependent effects and also to obtain the static moment capacity [29]. A data acquisition system was used to record the applied load and LVDT measurements during the tests, at one second intervals.

3.4 Initial distortional geometrical imperfections

The numerical investigation reported in [3] showed that distortional (critical-mode) initial geometrical imperfections are the most detrimental one in lipped channel beams susceptible to “true L-D interaction” when the local buckling is triggered by the top flange. Therefore, only the twin lipped channel specimen distortional initial geometrical imperfections (δ_D) were measured prior to testing. They were obtained for the mid-span cross-section only and their determination required measuring the distances between the web-flange corners (D – web width) and between the flange-lip corners (D_2 – including distortion), as shown in Fig. 2(b). The distortional displacements obtained ($\delta_D=D_2-D$) have been given in Table 2 – positive (negative) values indicate “outward” (“inward”) top flange-lip motions.

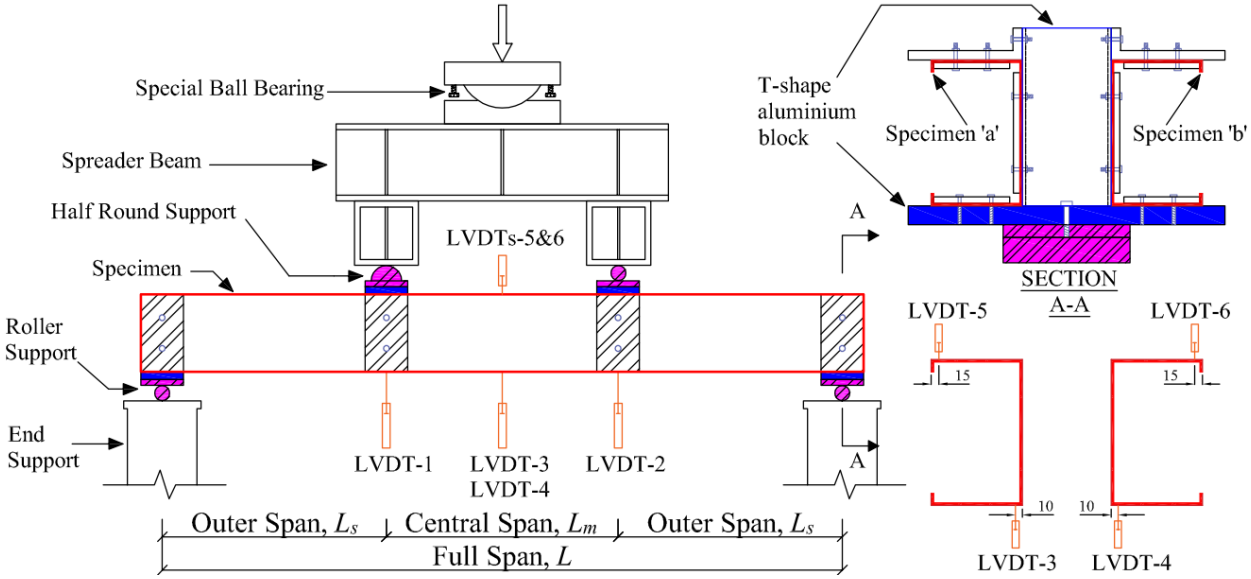

(a)

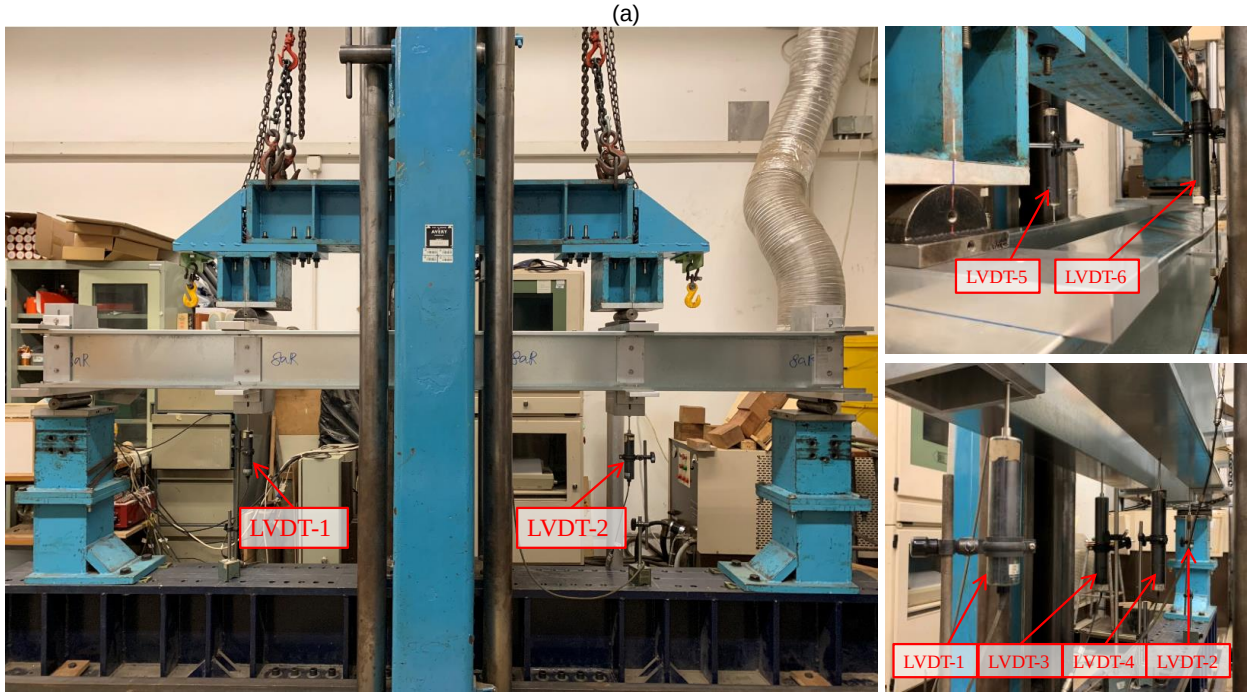

(b)

Figure 5: Four-point bending test rig and test set-up: (a) schematic representation and (b) overall views

3.5 Test results

The experimental results obtained from this test campaign are presented and discussed in the next two sub-sections – they consist of (i) photos showing the failure modes and corresponding failure moment values (Section 3.5.1), and (ii) moment-displacement equilibrium paths and photos showing deformed configurations along those equilibrium paths (Section 3.5.2). Since most of the specimens tested exhibited similar structural responses, only a representative fraction of the results obtained for the 40 beams (20 pairs) are presented and discussed in this work.

3.5.1 Failure modes and moments

Figs. 6(a)-(h) to 8(a)-(h) display photos of 25 specimen failure modes, *i.e.*, the deformed configurations at the onset of collapse. They concern specimens LC1-a+b, 3-a+b, 8R-a+b, 9-a+b, 10-a+b, 11-a+b, 12-b, 13-a+b, 14-a+b, 14R-a+b, 15-a+b, 17-a+b and 18-a+b. Moreover, the values of the 40 lipped channel beam experimental ultimate moments (M_{Exp}) obtained during this investigation are given in Table 4, together with the corresponding bending curvatures (κ_u) and distortional displacements at mid-span (Δ_D).

Table 4: Beam experimental failure moments, bending curvatures, distortional displacements and observed failure mode natures

Specimen	M_{Exp} (kNm)	κ_u (mm^{-1})	Δ_D (mm)	Failure mode nature
LC1-a	5.60	24.9	-20.3	L+D$^-$
LC1-b	5.60	8.3	-11.6	L+D$^-$
LC2-a	5.58	18.1	-15.6	L+D$^-$
LC2-b	5.58	22.8	-16.9	L+D$^-$
LC3-a	6.87	16.8	-21.8	L+D$^-$
LC3-b	6.87	18.3	17.2	L+D$^+$
LC4-a	6.45	14.8	-6.0	L+D$^-$
LC4-b	6.45	15.2	-8.9	L+D$^-$
LC5-a	5.35	16.6	-17.5	L+D$^-$
LC5-b	5.35	16.5	-17.2	L+D$^-$
LC6-a	7.46	13.5	-13.4	L+D$^-$
LC6-b	7.46	12.0	-17.9	L+D$^-$
LC7-a	7.09	13.5	-1.8	L+D$^-$
LC7-b	7.09	13.5	-3.1	L+D$^-$
LC8-a	8.77	12.6	-20.3	L+D$^-$
LC8-b	8.77	14.2	6.7	L+D$^+$
LC8R-a	8.01	14.3	-10.8	L+D$^-$
LC8R-b	8.01	11.4	-22.1	L+D$^-$
LC9-a	8.38	11.8	-23.9	L+D$^-$
LC9-b	8.38	9.4	-18.5	L+D$^-$
LC10-a	5.41	18.0	-16.1	L+D$^-$
LC10-b	5.41	16.9	-23.8	L+D$^-$
LC11-a	9.15	11.9	-23.3	L+D$^-$
LC11-b	9.15	10.4	-25.9	L+D$^-$
LC12-a	9.54	9.5	-20.1	L+D$^-$
LC12-b	9.54	11.7	6.7	L+D$^+$
LC13-a	10.65	9.2	-31.3	L+D$^-$
LC13-b	10.65	11.9	9.2	L+D$^+$
LC14-a	10.30	11.9	-23.8	L+D$^-$
LC14-b	10.30	11.4	4.8	L+D$^+$
LC14R-a	10.44	9.6	-26.7	L+D$^-$
LC14R-b	10.44	11.2	6.3	L+D$^+$
LC15-a	10.52	9.2	-16.3	L+D$^-$
LC15-b	10.52	10.3	-3.1	L+D$^-$
LC16-a	5.20	18.3	-5.6	L+D$^-$
LC16-b	5.20	17.0	-9.1	L+D$^-$
LC17-a	3.95	24.8	-9.8	L+D$^-$
LC17-b	3.95	22.6	-22.7	L+D$^-$
LC18-a	3.84	23.5	-29.6	L+D$^-$
LC18-b	3.84	24.5	-25.9	L+D$^-$

The photos presented in Figs. 6(a)-(h) to 8(a)-(h) provide very clear evidence that pronounced local and distortional deformations take place along the beam central span compressed (upper) regions, thus confirming that all these specimens experienced (true) L-D interaction. It is worth mentioning that the beam failures stem exclusively from the interaction between local and distortional buckling deformations, since no trace of shear or web-crippling deformations was observed in the beam outer spans and vicinity of the regions exhibiting high stress concentrations, respectively. As already mentioned, all the beams tested failed into local-distortional (L+D) interactive modes. All these failure modes exhibited a single distortional half-wave, involving either "outward" or "inward" top flange-lip motions. Table 4 identifies the beam specimens involving "outward" and "inward" top flange-lip motions by using the designations "L+D$^+$" or "L+D$^-$", respectively. In addition, note that the failure moment of the repeated specimens LC14R-a+b differs only by 1.35% from its "original" counterpart, thus indicating an excellent reliability of the test set-up and procedure. This excellent reliability is not "stained" by the 8.66% difference between the failure moments of specimens LC8R-a+b and LC8-a+b – this is because the lip widths of the former are visibly smaller (see Table 2), which provides a logical explanation for the lower failure moment. Finally, it was observed that all "twin" specimens (LC*-a and LC*-b) generally failed at the same time and, thus, exhibit virtually identical failure moments.

3.5.2 Equilibrium paths and additional deformed configurations

Figs. 9(a_1)-(c_4) show the equilibrium paths recorded during the performance of all the twin lipped channel beam tests. Each sub-figure contains 10 beam equilibrium paths: Figs. 9(a_1)-(c_1), Figs. 9(a_2)-(c_2), Figs. 9(a_3)-(c_3) and Figs. 9(a_4)-(c_4) concern beams LC-1-2-3-4-5, LC-6-7-8-8R-9, LC-10-11-12-13-14 and LC-14R-15-16-17-18, respectively. Every equilibrium path plots the applied moment M, obtained through the multiplication of the load value measured by the hydraulic actuator load cell P by L/16 (where the shear span was L/4), versus either (i) the bending curvature (Figs. 9(a_1)-(a_4)), determined by means of the equation

$$\kappa = \frac{2y}{\left(\frac{L}{4}\right)^2 + y^2} \qquad (1)$$

where $y=d_3-(d_1+d_2)/2$ or $y=d_4-(d_1+d_2)/2$ and d_1, d_2, d_3 and d_4 are the measurements of LVDT-1 to LVDT-4, respectively, (ii) the vertical deflection at mid span (Figs. 9(b_1)-(b_4)), measured by LVDT-3 or LVDT-4, and (iii) the distortional displacement at mid-span (Figs. 9(c_1)-(c_4)), given by the difference between the measurements of LVDT-5 and LVDT-3 (d_5-d_3) or LVDT-6 and LVDT-4 (d_6-d_4). On the other hand, Figs. 10(a)-(g) show illustrative beam deformed configurations after the collapse has been reached, *i.e.*, along the equilibrium path descending branch – they concern the specimen pairs LC1, LC2, LC5, LC8, LC9, LC14 and LC14R. The observation of the above beam equilibrium paths and deformed configurations leads to the following comments:

(i) With very few exceptions, the equilibrium path sets displayed in Figs. 9(a)+(b) are qualitatively similar and both exhibit a pronounced linear region. Indeed, is clear that the beam behavior remains practically linear (elastic) until the applied moment reaches the critical local buckling moment level. For instance, compare Figs. 9(b) with the critical local buckling moments given ahead, in Table 5 – note that (i_1) the elastic/yield moments are much higher than the critical local and distortional buckling moments, and that (i_2) local buckling always precedes distortional buckling.

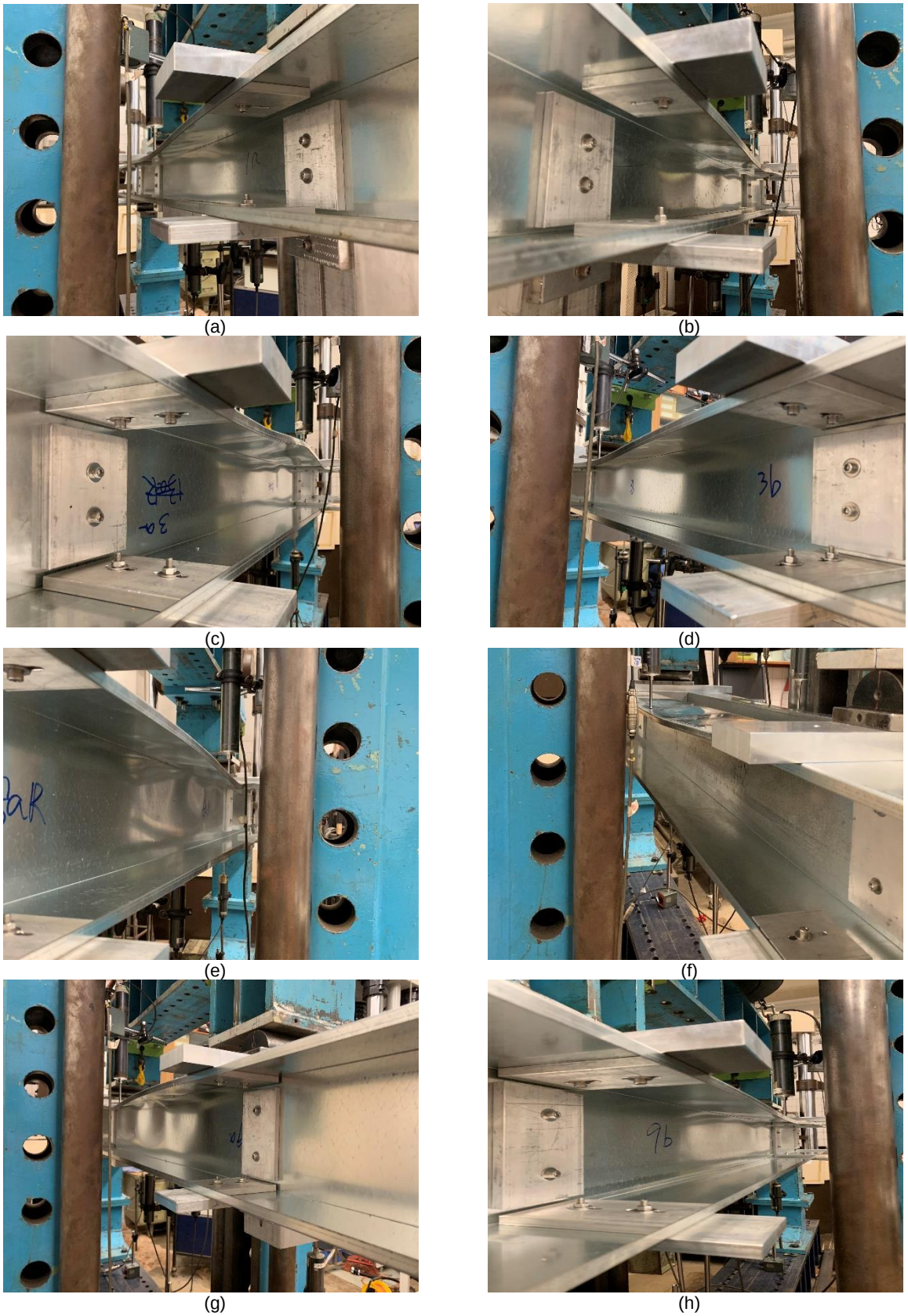

(a) (b) (c) (d) (e) (f) (g) (h)

Figure 6: L-D interactive failure modes of specimens (a) LC1-a, (b) LC1-b, (c) LC3-a, (d) LC3-b, (e) LC8R-a, (f) LC8R-b, (g) LC9-a and (h) LC9-b

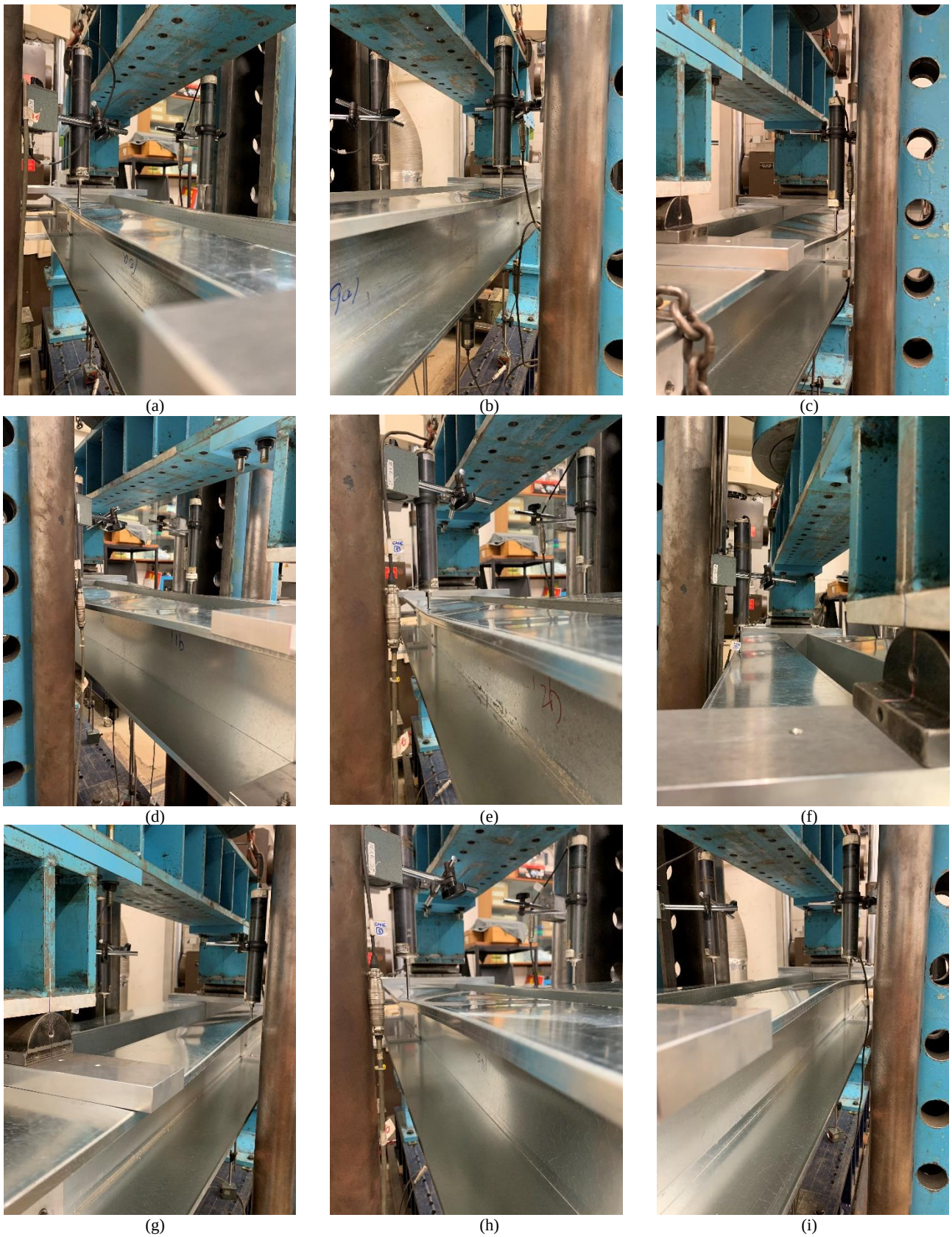

Figure 7: L-D interactive failure modes of specimens (a) LC10-a, (b) LC10-b, (c) LC11-a, (d) LC11-b, (e) LC12-b, (f) LC13-a, (g) LC13-b, (h) LC14-a and (i) LC14-b

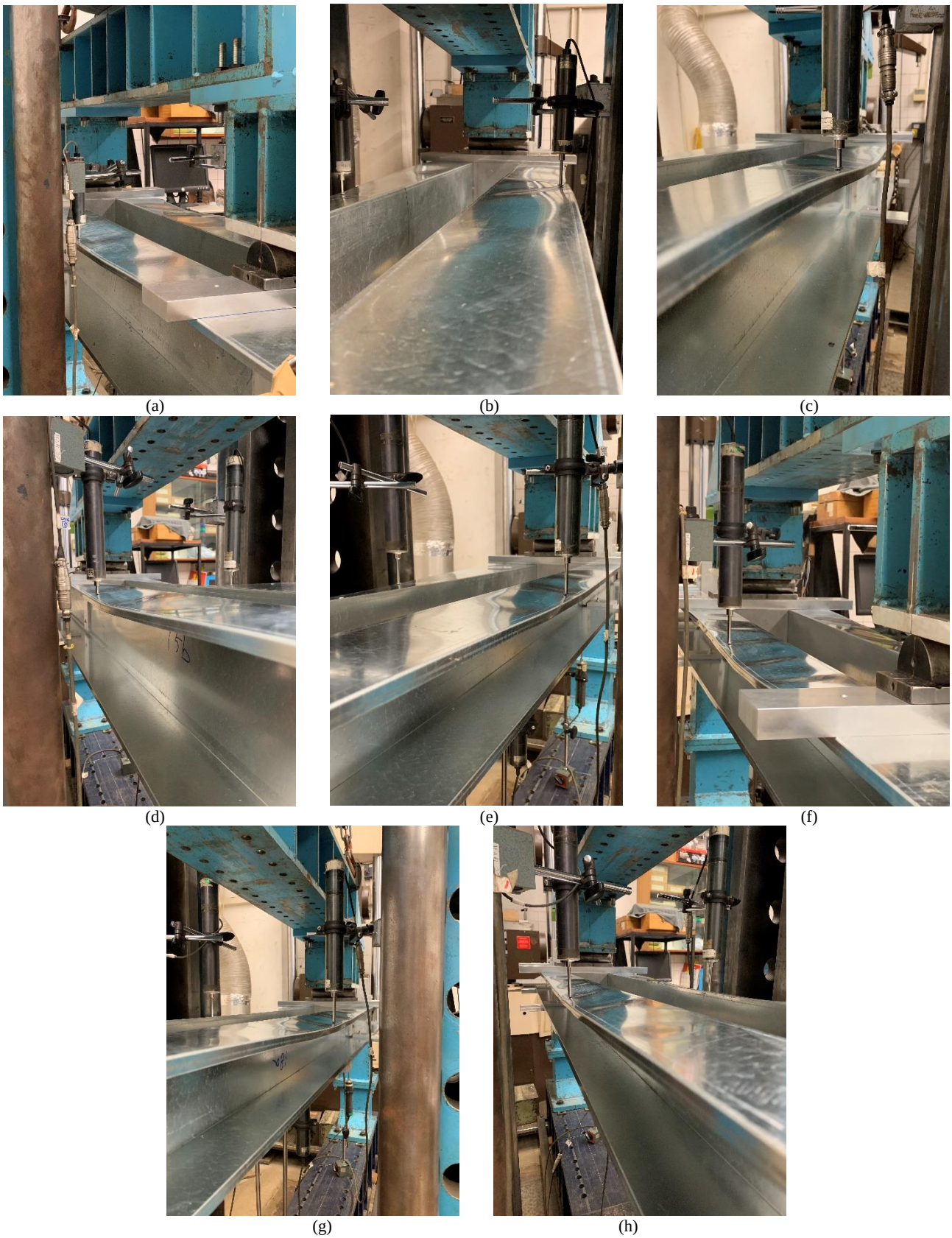

Figure 8: L-D interactive failure modes of specimens (a) LC14R-a, (b) LC14R-b, (c) LC15-a, (d) LC15-b, (e) LC17-a, (f) LC17-b, (g) LC18-a and (h) LC18-b

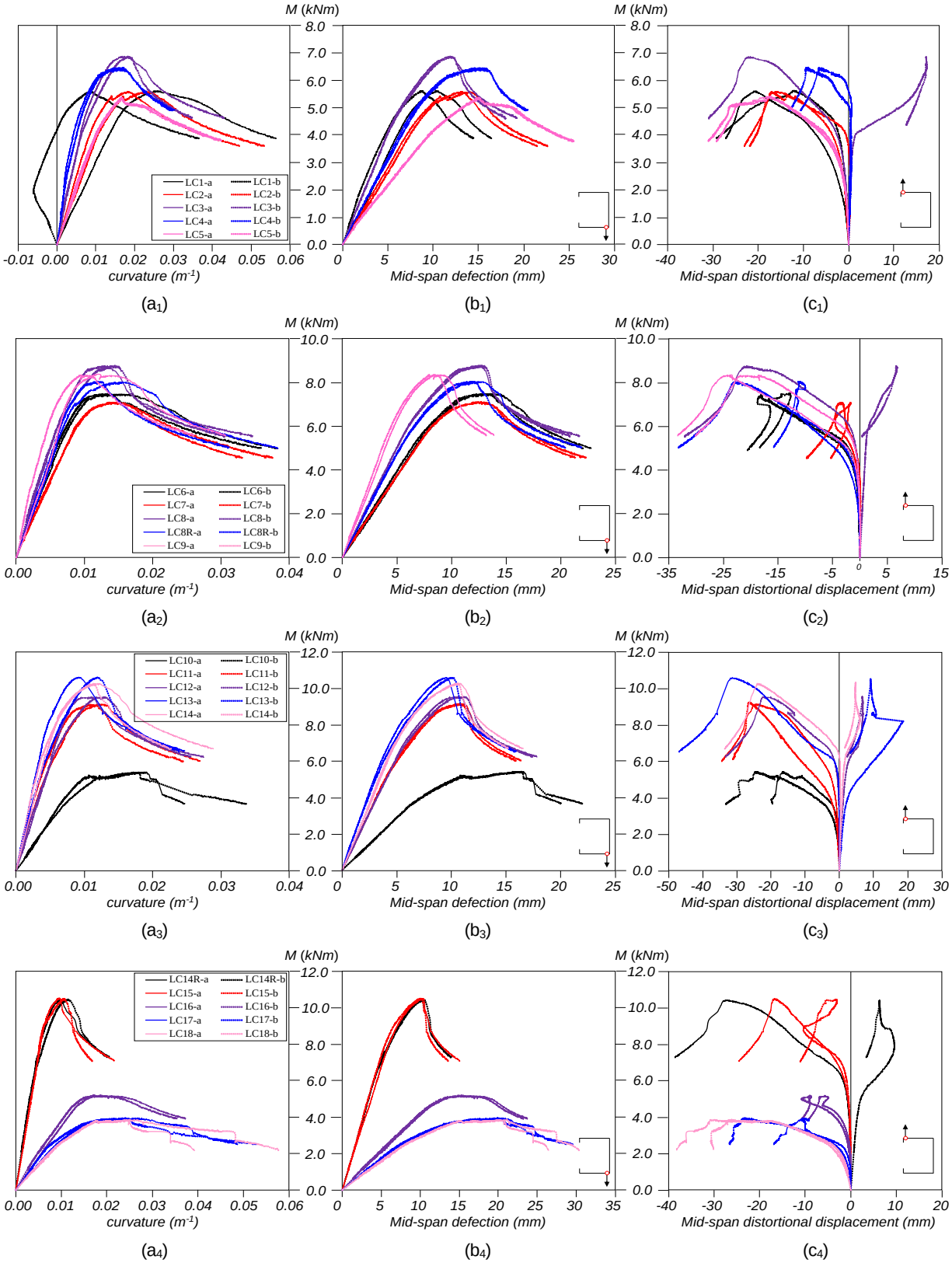

(a1) (b1) (c1)

(a2) (b2) (c2)

(a3) (b3) (c3)

(a4) (b4) (c4)

Figure 9: Experimental equilibrium paths *M* vs. (a) mid-span curvature, (b) mid-span bending defection and (c) mid-span distortional displacement, for specimens (1) LC1-2-3-4-5, (2) LC6-7-8-8R-9, (3) LC10-11-12-13-14 and (4) LC14R-15-16-17-18

(ii) The main differences between the twin lipped channel beam behaviors appear in the equilibrium paths shown in Figs. 9(c), which are strongly affected by the initial geometrical imperfections. In fact, in some twin beam specimens (*e.g.*, LC1, LC7, LC10, LC15 or LC17) these equilibrium paths are quite distinct – this is because the plastic hinge associated with the collapse mechanism (see item (iii)) develops at a different cross-section/region. Indeed, only for very few specimens (*e.g.*, LC5) are the equilibrium paths practically identical, a remarkable feature in view of the independent initial geometrical imperfections.

Figure 10: Beam deformed configurations after collapse (equilibrium path descending branch) of specimens (a) LC2, (b) LC8, (c) LC9, (d) LC14R, (e) LC1, (f) LC5 and (g) LC14

(iii) As was already mentioned, and illustrated in Figs. 6(a)-(h) to 8(a)-(h) and Table 4, the lipped channel beams exhibit either "inward" (mostly) or "outward" mid-span flange-lip motions. In addition, it was also observed the failure moments of the LC4, LC8, LC12, LC13, LC14 and LC14R twin beams, which exhibit opposite mid-span flange-lip motions (one "inward" and the other "outward"), are virtually identical. This means that, unlike in columns, there is practically no beam distortional post-buckling asymmetry with respect to the flange-lip motion sign, which provides clear experimental confirmation for the numerical findings reported in [3].

(iv) The post-collapse deformed configurations displayed in Figs. 10(a)-(g) show the development of "distortional plastic hinges" involving (iv_1) the full yielding of the compressed flange and half web, and also (iv_2) the appearance of "v-shaped" yield lines on the compressed flange. It is worth noting that these deformed configurations are quite similar to those obtained by means of shell finite element numerical simulations (*e.g.*, [3,12]). The only visible difference is the distortional plastic hinge location: exactly at mid-span in the numerical simulations and only in the close vicinity of the mid-span region in the tested specimens – in Figs. 10(a)-(g), the transducers location indicated the mid-span cross-section. Naturally, a logical explanation for this small discrepancy is the consideration of critical-mode (symmetrical) initial geometrical imperfections in the numerical simulations, while the tested specimens most likely exhibit distinct, irregular and non-symmetrical initial imperfection patterns. Moreover, Figs. 10(a)-(g) also show that, along the equilibrium path descending branch, the formation of the distortional plastic hinge "overpowers" the local deformations, which become barely visible at this stage – note that, at the onset of collapse, they are clearly visible, which can be confirmed by looking at Figs. 6(a)-(h) to 8(a)-(h). This behavioral feature has also been unveiled in the context of the shell finite element numerical simulations reported in [3].

(v) The difference between the test results of specimens LC1-a and LC1-b might be attributed to the fact that although the twin specimens are loaded at the same time through the load transfer block system, due to the presences of initial imperfections in the specimens, the load at the initial stage is mainly sustained by specimen LC1-a, which therefore leads to the existence of less deformation of specimen LC1-b at the middle of central span than that of specimen LC1-a.

4. Direct Strength Method (DSM) design

This section addresses the comparison between the experimental failure moments obtained during this investigation and their estimates provided by (i) the currently codified local (M_{nL}) and distortional (M_{nD}) DSM design curves, (ii) a recently proposed distortional DSM strength curve (M_{nD^*}) [13] and (iii) available DSM-based design approaches developed to handle beam L-D interactive failures (M_{nLD} and M_{nDL}) [12]. At this stage, it is worth mentioning that the first publication on the DSM dealt with cold-formed steel beams [32], which can then be viewed as the "birthplace" of this nowadays so widely popular and universally accepted design methodology. The five DSM-based failure moment estimates are provided by strength curves defined by the expressions

$$M_{nL}=\begin{cases} M_y+(1-C_{yl}^{-2})\left(M_p-M_y\right), & \lambda_L\le 0.776 \\ \left(1-0.15\lambda_L^{-0.8}\right)\lambda_L^{-0.8}M_y, & \lambda_L>0.776 \end{cases} \quad (2)$$

$$M_{nD}=\begin{cases} M_y+(1-C_{yd}^{-2})\left(M_p-M_y\right), & \lambda_D\le 0.673 \\ \left(1-0.22\lambda_D^{-1.0}\right)\lambda_D^{-1.0}M_y, & \lambda_D>0.673 \end{cases} \quad (3)$$

$$M_{nD^*}=\begin{cases} M_y+(1-C_{yd}^{-2})\left(M_p-M_y\right), & \lambda_D\le 0.673 \\ \left(1-0.23\lambda_D^{-1.55}\right)\lambda_D^{-1.45}M_y, & \lambda_D>0.673 \end{cases} \quad (4)$$

$$M_{nLD}=\begin{cases} M_{nD^*}, & \lambda_{LD}\le 0.776 \\ \left(1-0.15\lambda_{LD}^{-0.8}\right)\lambda_{LD}^{-0.8}M_{nD^*}, & \lambda_{LD}>0.776 \end{cases} \quad (5)$$

$$M_{nDL}=\begin{cases} M_{nL}, & \lambda_{DL}\le 0.673 \\ \left(1-0.23\lambda_{DL}^{-1.55}\right)\lambda_{DL}^{-1.45}M_{nL}, & \lambda_{DL}>0.673 \end{cases} \quad (6)$$

where (i) $\lambda_L=(M_y/M_{crL})^{0.5}$ and $\lambda_{LD}=(M_{nD^*}/M_{crL})^{0.5}$ are local slenderness values based on the yield moment and distortional bending strength, respectively, (ii) $\lambda_D=(M_y/M_{crD})^{0.5}$ and $\lambda_{DL}=(M_{nL}/M_{crD})^{0.5}$ are distortional slenderness values based on the yield moment and local bending strength, respectively, (iii) M_p is the cross-section plastic moment and (iv) C_{yl} and C_{yd} are parameters, dependent on λ_L and λ_D, respectively, that are involved in the determination of the inelastic strength reserve of the stocky beams (not relevant here since the beams are slender). To enable a comparison between the distinct strengths associated with the above five design curves, their values (M_{nL}/M_y, M_{nD}/M_y, M_{nD^*}/M_y, M_{nLD}/M_y, M_{nDL}/M_y) are plotted in Fig. 11 against the local/distortional slenderness, *i.e.*, under the assumption that the beams undergo "true L-D interaction" (R_{DL}=1.0).

Table 5 provides, for all the tested beam specimens, the (i) cross-section mid-line dimensions (b_w, b_f, b_l – web-flange-lip widths), (ii) span lengths (L), (iii) yield stresses (f_y) and major-axis yield moments (M_y), (iv) failure moments (M_{Exp}), (v) critical local (M_{crL}) and distortional (M_{crD}) buckling moments, obtained using the SFE model mentioned in Section 2 and based on the measured mid-line dimensions and determined elastic properties (see Table 3), (vi) critical distortional-to-local buckling moment ratio and (vii) distortional and local slenderness

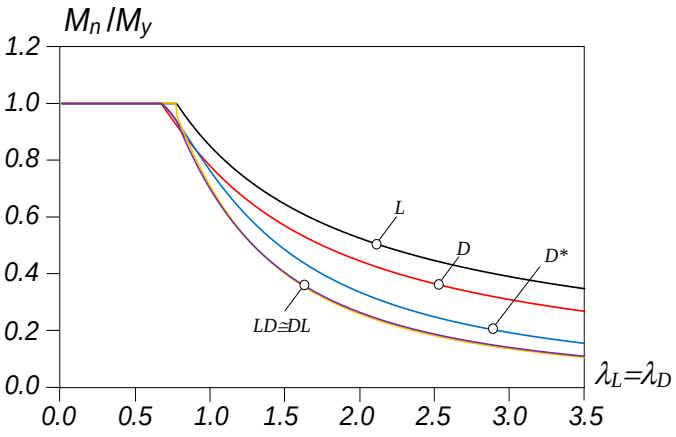

Figure 11: Plots of M_{nL}/M_y, M_{nD}/M_y, M_{nD^*}/M_y, M_{nLD}/M_y, M_{nDL}/M_y vs. $\lambda_L=\lambda_D$

values. Figs. 12(a)-(e) show plots of M_{Exp}/M_{nL} vs. λ_L, M_{Exp}/M_{nD} vs. λ_D, M_{Exp}/M_{nD^*} vs. λ_D, M_{Exp}/M_{nLD} vs. λ_L and M_{Exp}/M_{nDL} vs. λ_L for all the experimental failure moments obtained in this work. The observation of the plots depicted in Figs. 12(a)-(e) leads to the following comments:

(i) First of all, the comparison between the R_{DL} values of the planned and tested specimens, given in Tables 1 and 5, shows that the latter are a bit higher, which is exclusively due to the larger lip widths (the critical distortional buckling moments become larger).

(ii) A close inspection of the values presented in Table 5 provides experimental confirmation of some remarks made in [13], on the basis of numerical results. First, note that specimens with (almost) identical cross-sections exhibit very close failure moments M_{Exp} (and identical critical distortional half-wave numbers), regardless of the length – *e.g.*, compare the M_{Exp} values of specimens LC1-LC2.

Table 5: Beam specimen (i) cross-section mid-line dimensions, (ii) span lengths, (iii) yield stresses and moments, (iv) failure moments, (v) critical local and distortional buckling moments and their ratios, and (vi) local and distortional slenderness values

Specimen	b_w (mm)	b_f (mm)	b_l (mm)	t^* (mm)	L (mm)	f_y (MPa)	M_y (kNcm)	M_{Exp} (kNcm)	M_{crL} (kNcm)	M_{crD} (kNcm)	R_{DL} (-)	λ_L (-)	λ_D (-)
LC1-a	128.7	118.0	12.5	1.49	1800	490	1406	560	435	587	1.35	1.80	1.55
LC1-b	128.7	118.0	12.9	1.50	1800	490	1418	560	446	616	1.38	1.78	1.52
LC2-a	128.6	118.4	12.6	1.50	2200	490	1419	558	438	521	1.19	1.80	1.65
LC2-b	129.1	117.6	13.2	1.50	2200	490	1421	558	447	562	1.26	1.78	1.59
LC3-a	149.2	127.9	12.6	1.49	2200	490	1779	687	466	593	1.27	1.95	1.73
LC3-b	148.8	127.9	12.8	1.50	2200	490	1787	687	475	611	1.29	1.94	1.71
LC4-a	149.1	127.5	13.3	1.49	2600	490	1779	645	468	573	1.22	1.95	1.76
LC4-b	149.1	127.7	13.2	1.50	2600	490	1792	645	476	575	1.21	1.94	1.77
LC5-a	129.2	118.1	12.9	1.49	2600	490	1416	535	434	509	1.17	1.81	1.67
LC5-b	128.9	117.9	12.9	1.49	2600	490	1410	535	434	508	1.17	1.80	1.67
LC6-a	169.0	127.6	13.1	1.49	2600	490	2060	746	548	662	1.21	1.94	1.76
LC6-b	169.2	127.5	12.9	1.48	2600	490	2046	746	538	643	1.20	1.95	1.78
LC7-a	169.2	107.7	13.1	1.49	2600	490	1817	709	674	762	1.13	1.64	1.54
LC7-b	169.0	107.8	12.9	1.49	2600	490	1814	709	671	749	1.12	1.64	1.56
LC8-a	188.4	128.3	13.1	1.49	2600	490	2353	877	618	757	1.22	1.95	1.76
LC8-b	188.5	128.2	13.0	1.49	2600	490	2352	877	619	752	1.22	1.95	1.77
LC8-aR	188.7	128.4	12.1	1.49	2600	490	2348	801	613	690	1.13	1.96	1.84
LC8-bR	188.8	128.0	12.5	1.49	2600	490	2348	801	618	717	1.16	1.95	1.81
LC9-a	188.8	127.7	13.0	1.50	2200	490	2365	838	642	887	1.38	1.92	1.63
LC9-b	188.7	127.9	12.6	1.49	2200	490	2347	838	626	835	1.33	1.94	1.68
LC10-a	168.8	99.9	12.5	1.19	2600	614	1713	541	371	474	1.28	2.15	1.90
LC10-b	169.3	100.1	12.3	1.18	2600	614	1705	541	361	458	1.27	2.17	1.93
LC11-a	206.0	148.6	13.0	1.47	2600	490	2885	915	557	759	1.36	2.28	1.95
LC11-b	206.2	149.0	12.6	1.49	2600	490	2928	915	577	758	1.31	2.25	1.97
LC12-a	209.2	128.2	13.0	1.50	2600	490	2683	954	711	879	1.24	1.94	1.75
LC12-b	208.9	128.3	12.7	1.49	2600	490	2659	954	694	843	1.22	1.96	1.78
LC13-a	229.0	158.4	12.7	1.47	2600	490	3430	1065	588	859	1.46	2.42	2.00
LC13-b	229.3	157.8	12.8	1.48	2600	490	3450	1065	603	882	1.46	2.39	1.98
LC14-a	229.0	138.3	12.7	1.47	2600	490	3098	1030	678	906	1.34	2.14	1.85
LC14-b	229.0	138.1	12.5	1.49	2600	490	3134	1030	706	913	1.29	2.11	1.85
LC14-aR	229.0	137.6	12.7	1.48	2600	490	3108	1044	696	922	1.32	2.11	1.84
LC14-bR	228.9	137.6	12.6	1.49	2600	490	3125	1044	709	928	1.31	2.10	1.84
LC15-a	229.3	117.9	12.8	1.49	2600	490	2805	1052	831	1011	1.22	1.84	1.67
LC15-b	228.9	118.1	12.7	1.49	2600	490	2801	1052	828	999	1.21	1.84	1.67
LC16-a	128.9	108.2	12.6	1.48	2600	490	1309	520	479	523	1.09	1.65	1.58
LC16-b	128.9	108.1	12.6	1.48	2600	490	1308	520	479	523	1.09	1.65	1.58
LC17-a	129.7	109.9	12.3	1.18	2600	614	1332	395	238	321	1.35	2.37	2.04
LC17-b	128.9	109.8	12.5	1.20	2600	614	1345	395	249	336	1.35	2.33	2.00
LC18-a	128.1	99.7	12.9	1.20	2600	614	1242	384	280	382	1.37	2.11	1.80
LC18-b	128.6	99.8	12.5	1.19	2600	614	1236	384	273	363	1.33	2.13	1.85

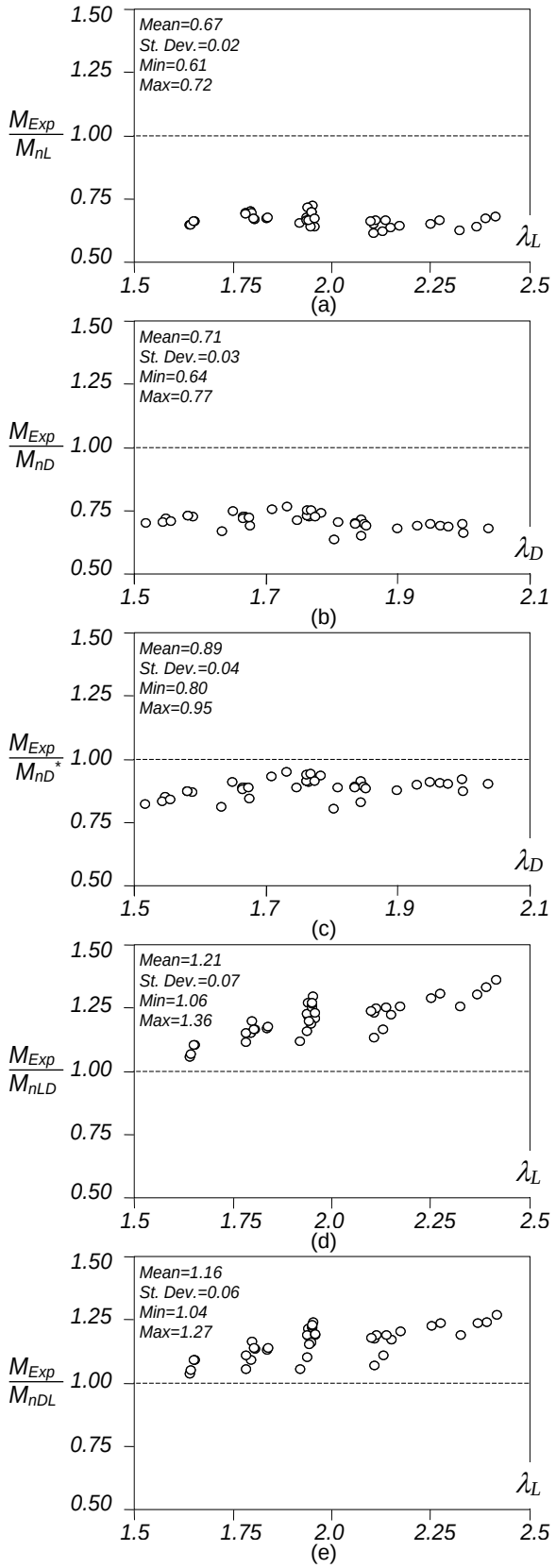

Figure 12: Plots (a) M_{Exp}/M_{nL} vs. λ_L, (b) M_{Exp}/M_{nD} vs. λ_D, (c) M_{Exp}/M_{nD^*} vs. λ_D, (d) M_{Exp}/M_{nLD} vs. λ_L and (e) M_{Exp}/M_{nDL} vs. λ_L for all the LC beam specimens tested

Finally, note also that specimens with higher b_w/b_f and/or b_f/b_l ratios exhibit larger failure moments – *e.g.*, compare the M_{Exp} values of specimens LC7-LC16 and LC6-LC17, respectively.

(iii) Generally speaking, the conclusions concerning the failure moment prediction quality of the various strength curves are in close agreement with those based on the numerical simulations reported in [12]. Indeed, as expected, the currently codified local and distortional DSM design curves provide very poor failure moment predictions (overestimations) for beams undergoing L-D interaction – mean values of M_{Exp}/M_{nL} and M_{Exp}/M_{nD} equal to 0.67 and 0.71, respectively. As for the distortional DSM strength curve proposed in [13], it provides less pronounced overestimations (higher M_{Exp}/M_{nD^*} ratios) than the codified one, but is also unable to adequately account the failure moment erosion due to L-D interaction – naturally, none of these three strength curves was developed with the purpose of taking into account for this failure moment erosion.

(iv) Not surprisingly, the DSM-based design approaches developed in [12] with the aim of handling beam L-D interactive failures are clearly those providing the best failure moment prediction quality – in addition, this quality is quite good. Indeed, Figs. 12(d)-(e) show that these strength curves always provide safe and fairly accurate predictions with low scatter, as attested by the statistical indicators included in these figures. Moreover, the M_{nDL} estimates slightly outperform their M_{nLD} counterparts: M_{Exp}/M_{nDL} and M_{Exp}/M_{nLD} mean and standard deviation equal to 1.16-0.06 and 1.21-0.07, respectively – note that, in both cases, the amount of overestimation increases with the slenderness.

(v) The experimental investigation reported by Ye *et al.* [21] led to several conclusions that are opposite to those reached in this work, which were presented in the previous items. For instance, these authors concluded that the M_{nL} and M_{nD} values provide good estimates of the experimental failure moments they obtained, which amounts to saying that L-D interaction causes no failure moment erosion and is in stark contrast with the plots depicted in Figs. 12(a)-(b). Consistently, the above authors also concluded that the M_{nDL} and M_{nLD} values excessively underestimate (by about 30% in average) the experimental failure moments, *i.e.*, underestimations much higher than those appearing in the plots depicted in Figs. 12(d)-(e). After carefully examining the work reported in [21], it was possible to identify several possible sources for the discrepancies, with respect to the present investigation, that were detected – they are described/addressed next:

(v_1) The beam tests reported involved "back-to-back" lipped channel specimens having the two webs in contact, which means that the failure modes mimic those exhibited by lipped I-section beams – this can

be clearly confirmed by looking at the failure modes reported in [21]. In the present investigation, the twin lipped channel beam specimens behave/deform almost independently.

(v_2) In about two thirds of the lipped channel cross-sections considered in [21] local buckling is triggered by the web, while in the present investigation local buckling is always triggered by the compressed flange. Earlier numerical work reported in [3] provided solid evidence that the failure moment erosion stemming from L-D interaction is much more relevant when local buckling is triggered by the compressed flange.

(v_3) The beam critical local and distortional buckling moments, required to obtain the slenderness values involved in evaluating the various DSM failure moment predictions, were determined by means of the CUFSM code, considering isolated lipped channel beams (not lipped I-section beams with a double web thickness) exhibiting ideal support and loading conditions. For instance, doubling the web thickness may alter significantly the critical local and distortional buckling moments. Moreover, the critical local and distortional buckling moments employed in [21] were the minimum values of simply supported beam "signature curves" – recall that, in the present investigation, the critical local and distortional buckling moments were calculated by means of a shell finite element models simulating, as closely as possible, the actual test set-up.

(vi) Finally, it should be mentioned that the experimental results presented in this work provide solid evidence about the need to equip the cold-formed steel technical/scientific community with an efficient (safe, accurate and reliable) DSM-based design approach able to capture adequately the failure moment erosion due to L-D interaction. Although it appears that the M_{nDL} and M_{nLD} failure moment estimates are well-positioned candidates for such role, further (experimental and numerical) validation is still necessary before a proposal for codification can be made. In particular, beams with other cross-section shapes must also be considered.

5. Conclusions

This work reported an experimental investigation, planned at the University of Lisbon and carried out at The University of Hong Kong, aimed at investigating the behavior and strength of CFS lipped channel beams undergoing L-D interaction and gathering a fairly substantial failure moment set concerning beams affected by this coupling phenomenon. After presenting an updated review of the available literature on this topic, the paper addressed the buckling analyses required to perform the beam geometry selection, intended to identify lipped channel beams exhibiting different critical distortional-to-local buckling moment ratios, all associated with the occurrence of local-distortional interaction. This selection procedure led to the performance of 20 four-point (major-axis) bending tests, each involving a pair of (twin) lipped channel beams placed in a "back-to-back" configuration – in other words, 40 lipped channel beams laterally restrained at the loading points (L/4 far away from the supports) were tested. After addressing the tensile coupon tests, performed to characterize the material properties of the steel batches used to manufacture the beam specimens, the paper described in detail the test set-up and procedure, including the location of the LVDTs employed to measure the initial geometrical imperfections, prior to the tests, and to record key mid-span displacements, during the tests. Then, the experimental results obtained were presented and discussed – they consisted of (i) non-linear moment-displacement equilibrium paths, (ii) photos showing deformed configurations along those paths (including the failure modes) and (iii) failure moments. Finally, the paper provided a comparison between the experimental failure moments obtained in this work with their estimates provided by five DSM-based strength curves, namely (i) the currently codified local and distortional design curves, (ii) a distortional strength curve proposed in [13] and (iii) two strength curves recently developed to handle beam local-distortional (L-D) interactive failures [12].

As planned, all the 40 lipped channel beams tested, exhibiting critical distortional-to-local buckling moment ratios comprised between 1.09 and 1.46, experienced significant L-D interaction. Thus, it was possible to obtain experimental evidence of this coupling phenomenon, as well as to gather a fairly large set of experimental failure moments of beams affected by L-D interaction, which are scarcely available in the literature. The experimental results obtained in this work were found to be in very good agreement with recently performed numerical simulations – for instance, there is a striking resemblance between the moment-displacement equilibrium paths and collapse mechanisms (including the associated plastic hinge locations). Moreover, it was also possible to confirm the negligible distortional post-buckling asymmetry (unlike in columns undergoing L-D interaction), the dominant role played by the distortional deformations (over the local ones) and the influence of the cross-section dimensions on the failure moment.

The comparison between the experimental failure moments obtained and their predictions provided by the aforementioned five DSM-based strength curves provided solid evidence of the need to include in the cold-formed steel specifications a design approach specifically intended to handle beam L-D interactive failures[7]. Indeed, an acceptable failure moment prediction quality could only be achieved by the estimates provided by the

[7] Although this conclusion appears to contradict the findings recently reported by Ye *et al.* [21], it was possible to identify several possible sources for the apparent discrepancies between the two sets of experimental results. This issue will be further addressed by the authors in the near future.

two DSM-based design approaches developed specifically to handle L-D interactive failures – one of them (M_{nDL}) slightly outperforms the other (M_{nLD}). Although it is undeniable that further experimental and numerical investigation is still needed, it seems fair to argue that the M_{nLD} design approach will provide a good basis for searching an efficient DSM-based design approach for cold-formed steel beams failing in L-D interactive modes that can be proposed for codification – the authors are currently working towards achieving this goal and will soon report the output of this research effort.

6. Acknowledgments

The authors gratefully acknowledge the support of M Metal Pte Ltd in Singapore, for supplying the cold-formed steel beam specimens tested at The University of Hong Kong.

References

[1] Camotim D., Dinis P.B., Martins A.D., Young B., Review: interactive behaviour, failure and DSM design of cold-formed steel members prone to distortional buckling, *Thin-Walled Structures*, 128(July), 12-42, 2018.

[2] Silvestre N., Dinis P.B., Camotim D., Direct strength method for lipped channel columns and beams affected by local-plate/distortional interaction, *Proceedings of 18th International Specialty Conference on Cold-Formed Steel Structures* (Orlando, 26-27/10), W.-W. Yu, R. Laboube (eds.), 17-37, 2006.

[3] Dinis P.B., Camotim D., Local/distortional mode interaction in cold-formed steel lipped channel beams, *Thin-Walled Structures*, 48(10-11), 771-785, 2010.

[4] Anbarasu M., Local-distortional buckling interaction on cold-formed steel lipped channel beams, *Thin-Walled Structures*, 98B(January), 351-359, 2016.

[5] AISI (American Iron and Steel Institute). North American Specification (NAS) for the Design of Cold-Formed Steel Structural Members (AISI-S100-16) + respective Commentary, Washington DC, USA, 2016.

[6] Haidarali M.R., Nethercot D.A., Finite element modelling of cold-formed steel beams under local buckling or combined local/distortional buckling, *Thin-Walled Structures*, 49(12), 1554-1562, 2011.

[7] Yu C., Schafer B.W., Local buckling tests on cold-formed steel beams, *Journal of Structural Engineering* (ASCE), 129(12), 1596-1606, 2003.

[8] Yu C., Schafer B.W., Distortional buckling tests on cold-formed steel beams, *Journal of Structural Engineering* (ASCE), 132(4), 515-528, 2006.

[9] Haidarali M.R., Nethercot D.A., Local and distortional buckling of cold-formed steel beams with both edge and intermediate stiffeners in their compression flanges, *Thin-Walled Structures*, 54(May), 106-112, 2012.

[10] Haidarali M.R., Nethercot D.A., Local and distortional buckling of cold-formed steel beams with edge-stiffened flanges, *Journal of Constructional Steel Research*, 73(June), 31-42, 2012.

[11] Schafer B.W., Cold-Formed Steel Behavior and Design: Analytical and Numerical Modeling of Elements and Members with Longitudinal Stiffeners, Ph.D. Thesis, Cornell University, Ithaca (NY), USA, 1997.

[12] Martins A.D., Camotim D., Dinis, P.B., Local-distortional interaction in cold-formed steel beams: behaviour, strength and DSM design, *Thin-Walled Structures*, 118(October), 879-901, 2017.

[13] Martins A.D., Landesmann A., Camotim D., Dinis P.B., Distortional failure of cold-formed steel beams under uniform bending: behaviour, strength and DSM design, *Thin-Walled Structures*, 118(September), 196-213, 2017.

[14] Martins A.D., Camotim D., Gonçalves, R., Dinis, P.B., On the mechanics of local-distortional interaction in thin-walled lipped channel beams, *Thin-Walled Structures*, 128(July), 108-125, 2018.

[15] Bernard E.S., Bridge R.Q., Hancock G.J., Tests of profiled steel decks with v-stiffeners, *Journal of Structural Engineering* (ASCE), 119(8), 2277-2293, 1993.

[16] Bernard E.S., Bridge R.Q., Hancock G.J., Tests of profiled steel decks with flat-hat stiffeners, *Journal of Structural Engineering* (ASCE), 121(8), 1175-1182, 1995.

[17] Wang H., Zhang Y., Experimental and numerical investigation on cold-formed steel C-section flexural members, *Journal of Constructional Steel Research*, 65(May), 1225-1235, 2009.

[18] Wang L., Young B., Design of cold-formed steel channels with stiffened webs subjected to bending, *Thin-Walled Structures*, 85(December), 81-92, 2014.

[19] Douty R.T., A design approach to the strength of laterally unbraced compression flanges, Bulletin 37, *Engineering Experiment Station*, Cornell University, Ithaca, NY, USA, 1962.

[20] Serrette R.L., Peköz T., Distortional buckling of thin-walled beams/panels. II: Design methods, *Journal of Structural Engineering* (ASCE), 121(4), 767-776, 1995.

[21] Ye J., Meza F.J., Hajirasouliha I., Becque J., Shepherd P., Pilakoutas K., Experimental investigation of cross-sectional bending capacity of cold-formed steel channels subjected to local-distortional buckling interaction, *Journal of Structural Engineering* (ASCE), 145(7), 0401964 (15 pages), 2019.

[22] Schafer B.W., Review: the direct strength method of cold-formed steel member design, *Journal of Constructional Steel Research*, 64(7-8), 766-778, 2008.

[23] Camotim D., Dinis P.B., Martins A.D., Direct Strength Method (DSM) – a general approach for the design of cold-formed Steel structures, Recent Trends in Cold-Formed Steel Construction, C. Yu (ed.), Woodhead Publishing

(Series in Civil and Structural Engineering), Amsterdam, 69-105, 2016.

[24] Schafer B.W., Advances in the Direct Strength Method of cold-formed steel design, *Thin-Walled Structures*, 140(July), 533-541, 2019.

[25] CEN (Comité Européen de Normalisation), Eurocode 3: Design of Steel Structures – Part 1-5: Plated Structural Elements, EN 1993-1-5:2006, Brussels, Belgium, 2006.

[26] CEN (Comité Européen de Normalisation), Eurocode 3: Design of Steel Structures – Part 1-3: General Rules; Supplementary Rules for Cold-Formed Members and Sheeting, EN 1993-1-3:2006, Brussels, Belgium, 2006.

[27] Simulia, Inc., ABAQUS Standard (version 6.7-5), 2008.

[28] AS 1397. Continuous Hot-Dip Metallic Coated Steel Sheet and Strip – Coatings of Zinc and Zinc Alloyed with Aluminium and Magnesium, AS 1397-2011, Sydney, Australia, 2011.

[29] ASTM-E8M. Standard test methods for tension testing of metallic materials, ASTM E8M-16, West Conshohocken, PA, USA, 2016.

[30] Huang Y., Young B., The art of coupon tests, *Journal of Constructional Steel Research,* 96(May), 159-175, 2014.

[31] Chen M.-T., Young, B., Martins A.D., Camotim D., Dinis P.B., Experimental investigation on cold-formed steel stiffened lipped channel columns undergoing local-distortional, *Thin-Walled Structures*, 150(May), paper 106682 (20 pages), 2020.

[32] Schafer B.W., Peköz T., Direct strength prediction of cold-formed steel members using numerical elastic buckling solutions, *Proceedings of 14th International Specialty Conference on Cold-Formed Steel Structures* (St. Louis, 15-16/10), W.-W.Yu, R. Laboube (eds.), 69-76, 1998